Geometrico-Static Analysis of a New Collaborative Parallel Robot for Safe Physical Interaction

Guillaume Jeanneau, Vincent Begoc, Sébastien Briot

**Proceedings of the ASME 2020 International Design Engineering Technical Conferences &
Computers and Information in Engineering Conference
IDETC/CIE 2020
August 16-19, 2020, St. Louis, USA**

DETC2020/xxxx

GEOMETRICO-STATIC ANALYSIS OF A NEW COLLABORATIVE PARALLEL ROBOT FOR SAFE PHYSICAL INTERACTION

Guillaume Jeanneau[a,b,*] **Vincent Bégoc**[a,c] **Sébastien Briot**[a,d]

[a] Laboratoire des Sciences du Numérique de Nantes (LS2N)
UMR CNRS 6004, 44321 Nantes, France
[b] École Centrale de Nantes
[c] Institut Catholique d'Arts et Métiers (Icam)
[d] Centre National de la Recherche Scientifique (CNRS)
Emails: {Guillaume.Jeanneau,Sebastien.Briot}@ls2n.fr, Vincent.Begoc@icam.fr

ABSTRACT

This paper introduces a geometrico-static analysis of an intrinsically safe parallel manipulator called R-Min. This robot was designed to reduce the risk of injury during a collision with a human operator, thanks to an underactuated architecture which enables large internal displacements in case of a collision. Indeed, the R-Min architecture is based on a modification of the well-known planar five-bar mechanism, where additional passive joints are introduced on the distal links in order to create a planar seven-bar mechanism with two degrees of underactuation. These two additional degrees of freedom are passively driven through the use of a supplementary passive leg, in which a tension spring is mounted between the base and the end-effector.

In this paper, the conditions satisfying the equilibrium and the stability of the mechanism are introduced, based on a geometrico-static analysis. The direct and inverse problems are then solved using a numerical approach. Solutions to both problems are presented and classified. One subset of solutions to the inverse problem is isolated and projected in the Cartesian space in order to obtain the payload-invariant workspace of the R-Min robot.

*Address all correspondence to this author.

1 INTRODUCTION

Collaborative robots are intended to help humans with arduous working situations. Operating in the vicinity of human beings requires robots to evolve in highly dynamic environment and deal with unpredictable behaviour of operators while ensuring their safety in case of unavoidable human-robot collision.

Avoiding human injuries can be achieved through the use of proprioceptive force sensing technologies allowing the detection of collision and the appropriate reaction of the robot defined by the controller (see [1] for a survey of collision detection and control strategies). However, although being able to detect a collision, conventional robots must operate at low-speed, due to their high mass and inertia, in order to fulfill the energy thresholds given in the standard ISO/TS 15066 [2]. This document gives the maximal energy that can be transferred to various body regions and would result in a potential minor injury, in case of a transient contact (i.e. a collision in unconstrained space). Other strategies are based on exteroceptive sensors allowing to anticipate dangerous situation and adapt the robot's behaviour with respect to the operator's proximity [3]. In practice, this approach relies on algorithms that are hard to certify.

The drawbacks of the control approach highlight the need for intrinsically safe robots through proper mechanical design. This can be achieved by designing robots with lighter architecture [4,5]. However, these robots remain stiff and must operate at

low-speed to be able to react fast enough to a collision. A complementary approach consists in using compliant joints to reduce the peak force during a collision. This can be achieved using serial elastic actuators (SEA) [6], or preferably, variable stiffness actuators (VSA) [7–10], whose stiffness can be adapted to different kind of tasks and keep a safe behaviour. However VSA integrate small actuators and thus lead to complex, heavy and costly mechanisms. Another approach consists in using torque limiters [11–14], that offer precise positioning in a normal operating mode, while allowing disengagement when a torque threshold is exceeded due to a collision. Such torque limiters have been for instance installed between a suspended manipulator and its end-effector in [15]. Recently, a collaborative parallel robot for pick-and-place tasks was introduced in [16]. It is based on a regular five-bar mechanism whose distal links are made of soft material so that they can deform in case of collision. Despite the interest of this concept, collisions with the robot were not simulated nor experimented making it difficult to conclude on the benefits from a safety point a view.

In a previous paper [17], we introduced the R-Min robot whose architecture is based on the well-known planar five-bar mechanism, where additional passive joints are introduced to the distal links. The obtained mechanism is a planar seven-bar mechanism with two degrees of underactuation, authorizing the robot to passively self-reconfigure in case of collision. A supplementary passive leg, in which a tension spring is mounted, is added between the base and the end-effector in order to constrain the additional degrees of freedom. Simulations were conducted in order to analyze the impact force and the HIC (Head Injury Criteria) [18] during a collision with the head of an operator at high-speed (> 1.2 m/s). The results of these simulations showed that R-Min is intrinsically much safer than a regular rigid five-bar mechanism.

The purpose of the present paper is (i) to investigate the computation of the forward and inverse geometrico-static problems of the R-Min robot and (ii) analyze its workspace properties. As a result, the paper is divided as follows. Section II introduces the robot architecture and recalls its behaviour under the application of several types of loadings. Section III explains the resolution of the the forward and inverse geometrico-static problems. Indeed, because the robot is under-actuated, its equilibrium configurations are necessarily defined by both the geometric and the statics equations. In Section IV, we analyze the joint and Cartesian robot spaces, and identify solutions to the direct and inverse geometrico-static problems. Finally, in Section V, conclusions are drawn.

2 PRESENTATION OF THE ROBOT

2.1 Description of the kinematic architecture

R-Min robot, presented in Fig. 1(a), is based on a modified five-bar parallel mechanism, which is widely used for pick-and-place operations at high speed [19]. This five-bar mechanism (Fig. 1(b)) is a parallel robot made of two actuated revolute joints located at points O_{i1} ($i = 1,2$), and three passive revolute joints at points O_{12}, O_{22} and P. All joint axes are normal to the vertical plane $\mathscr{P}_0 : (A, \mathbf{x}_0, \mathbf{z}_0)$. This robot has two degrees of freedom (dof), two motors, and is then fully actuated and able to position the point P in the plane $\mathscr{P}_0$ with a high rigidity. While being able to perform at high-speed/high-accelerations (15 G of acceleration at the end-effector [19]), it is unable to collaborate with humans because of its high impedance.

As a result, in order to conserve the interesting speed properties while decreasing its impedance, we propose to modify the architecture of the five-bar mechanism as shown in Fig. 1(a). R-Min robot is thus composed of:

- a seven-bar parallel mechanism, with two actuated revolute joints located at points O_{i1}, and five passive revolute joints at points O_{i2}, O_{i3} and P ($i = 1,2$). All joint axes are normal to the vertical plane $\mathscr{P}_0 : (A, \mathbf{x}_0, \mathbf{z}_0)$. This mechanism has four dof (instead of two for the five-bar mechanism), but only two motors. It is thus underactuated, with two unconstrained dofs. This seven-bar mechanism is thus of little practicability due to its null stiffness.
- therefore, we add a preload system made of a kinematic chain located between points A and P, which is composed of two passive revolute joints at A and P, whose axis are normal to the plane $\mathscr{P}_0$, a passive prismatic joint aligned along $\overrightarrow{AP}$ lying in $\mathscr{P}_0$, and a compression spring exerting a compressing effort between points A and P. This preload system plays the same role as elastic elements introduced in the design of underactuated hands [20], i.e. it is added here in order to passively drive the unconstrained dofs of the robot and to kinematically constrain its configuration. Preloaded springs could have been installed on one passive joint of the seven-bar mechanism, but this would have increased the mass of bodies that are likely to collide with an operator. The selected solution of a preload bar located inside the two legs of the seven-bar mechanism is safer, since it does not allow the operator to collide with this bar and in the same time permits to obtain a lightweight design of the external legs.

Indeed, this preload system is able to tense the passive underactuated chain O_{12}, O_{13}, P, O_{23}, O_{22}, which is then more rigid than in the case of the single seven-bar mechanism. However, it will have much less stiffness than a traditional five-bar mechanism, thus making it a good candidate for a collaborative parallel robot.

2.2 Description of the concept

In Fig. 2, the equilibrium of the robot is shown for different types of efforts applied on the robot. It appears that, when the robot is subject to gravity effects only or with an additional

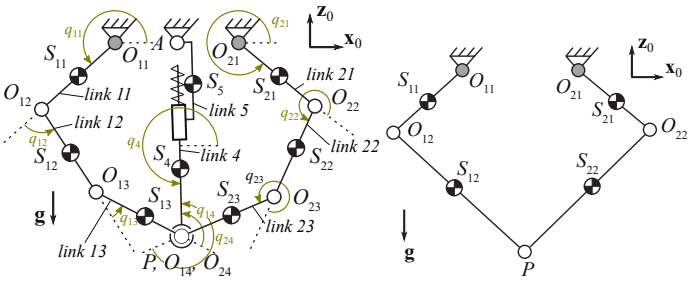

(a) R-min robot (b) A five-bar mechanism

FIGURE 1: Kinematic chains of (a) R-Min robot, (b) a five-bar mechanism. Grey joints are the active joints.

vertical force applied at the end-effector P and directed downwards (Fig. 2(a)) (equivalently to the robot payload), points O_{i2}, O_{i3} and P are near to be aligned, i.e. spring plus the external loadings tense the passive bars. When a force with an upward component is applied either at the end-effector P or on a passive link (Fig. 2(b-c)), which would be equivalent to forces appearing during an impact (Fig. 2(d)), the robot encounters large displacements of its bodies during its internal reconfiguration. As a result, when the robot is subject to types of loadings appearing during the manipulation of objects (i.e. downward forces), the end-effector location is close to the one that would be attained by a five-bar mechanism with distal links whose lengths are equal to $\ell_{O_{i2}O_{i3}} + \ell_{O_{i3}P}$, which is convenient for pick-and-place operations planning. On the contrary, when the robot is subject to types of loadings appearing during an impact with a human (i.e. forces with an upward component), the robot encounters large internal reconfigurations and is thus likely to avoid transmitting a large part of its energy during impact thanks to this reconfiguration. These properties makes him a good candidate for safe physical interactions during pick-and-place operations.

It should also be noted that the analysis of several configurations showed that displacements of the point on which the force is applied are bigger when the force is applied on the distal links (Fig. 2(d)) rather than on the end-effector (Fig. 2(c)). So intuitively, an impact on the links may lead to less energy transmission during collision than an impact on the end-effector. This behavior was shown in the simulations performed in [17].

In what follows, we denote as:

- $\mathbf{q}_a = \begin{bmatrix} q_{11} & q_{21} \end{bmatrix}^T$ the vector of the active joint coordinates representing the motion of the motors located at O_{11} and O_{21},
- $\mathbf{q}_d = \begin{bmatrix} q_{12} & q_{13} & q_{22} & q_{23} \end{bmatrix}^T$ the vector of passive joint coordinates,
- $\mathbf{p} = \begin{bmatrix} x & z \end{bmatrix}^T$ the position of point P, which is the end-effector location.
- q_4 the angle between axis $\mathbf{x}_0$ and the preload bar.
- $\rho_5 = \|\overrightarrow{AP}\| = \sqrt{x^2 + z^2}$ is the length of the preload system.

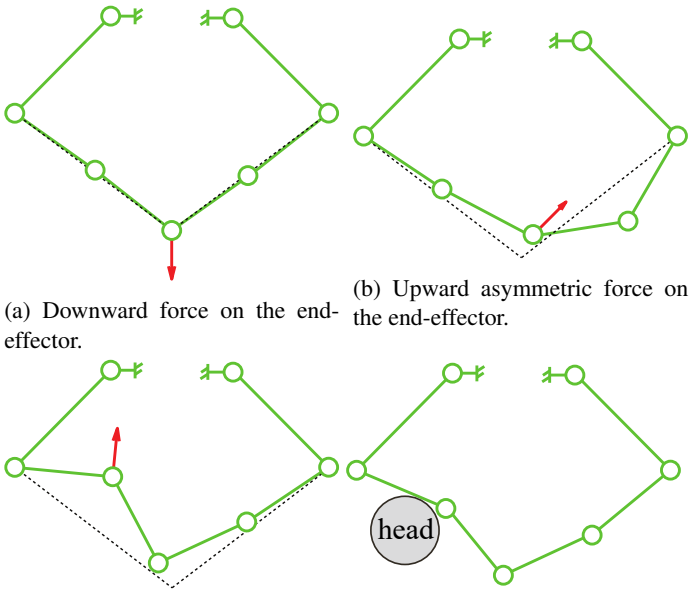

(a) Downward force on the end-effector.

(b) Upward asymmetric force on the end-effector.

(c) Force applied on the medial joint.

(d) A human head collides with the robot.

FIGURE 2: Representation of equilibrium configurations of the R-Min robot when subject to different types of external forces. The robot self-configures in case of a collision with a human.

3 GEOMETRICO-STATIC ANALYSIS

Unlike conventional robots, the equilibrium configuration of the R-Min robot does not only rely on the geometric constraints but also on gravitational effects, external forces and stiffness of the preloaded spring. This is due to the presence of unconstrained degrees of freedom in the mechanism. In the following, we present a method to solve the Direct Geometrico-Static Problem (DGSP), based on the minimization of the potential energy of the system. We then investigate the Inverse Geometrico-Static Problem (IGSP), i.e. we determine the control input $\mathbf{q}_a$ for a desired position $\mathbf{p}$. In both cases, the stability of the obtained equilibrium configurations is also considered.

3.1 Direct Geometrico-Static Problem (DGSP)

Solving the DGSP consists in finding all configurations $\mathbf{q}_t = \begin{bmatrix} \mathbf{p}^T & \mathbf{q}_d^T \end{bmatrix}^T$ that minimize the potential energy of the system and verify the geometric constraints for a given set of the active joint coordinates $\mathbf{q}_a$. This can be formulated as a classical optimization problem. In what follows, we assume no friction in the joints and the robot is assumed to be in static conditions.

Potential energy model The potential energy of the robot is computed from the potential energy $U_{i,j}$ of the links (i, j) $(i = 1, 2,\ j = 1, 2, 3)$. It depends on the mass m_{ij}, the position of

the center of inertia S_{ij} and the lengths ℓ_{ij} of the different links. The gravity field is denoted as g. We assume the points O_{ij}, S_{ij} and O_{ij+1} are aligned and we denote as ℓ_{Sij} the length $\|\overrightarrow{O_{ij}S_{ij}}\|_2$. For the compressive leg (respectively, for the prismatic joint), ℓ_{S4} is the distance from point P to its center of gravity S_4 (respectively, ℓ_{S5} is the distance from point A to its center of gravity S_5), m_4 (respectively m_5) is its mass, U_4 (respectively U_5) its potential energy. As a result, we have for $i = 1, 2$:

$$U_{i,1} = g m_{i1} \ell_{Si1} \sin(q_{i1}), \tag{1}$$
$$U_{i,2} = g m_{i2} \left(\ell_{i1} \sin(q_{i1}) + \ell_{Si2} \sin(q_{i1} + q_{i2})\right) \tag{2}$$
$$U_{i,3} = g m_{i3} \left(\ell_{i1} \sin(q_{i1}) + \ell_{i2} \sin(q_{i1} + q_{i2}) + \ell_{Si3} \sin(q_{i1} + q_{i2} + q_{i3})\right) \tag{3}$$
$$U_4 = g m_4 z (1 + \ell_{S4}/\rho_5) \tag{4}$$
$$U_5 = g m_5 \ell_{S5} \sin(q_4) \tag{5}$$

The energy of the spring U_s is moreover calculated from the spring stiffness k and its free length ℓ_0:

$$U_s = \frac{1}{2} k \left(\sqrt{x^2 + z^2} - \ell_0\right)^2 \tag{6}$$

We consider a constant payload $\mathbf{f}$ applied on the end-effector. Different loci of application of the external force could be considered but are out of the scope of this paper. This force is assumed conservative and its potential function is added to the total potential energy:

$$U = \sum_{i=1}^{2} \sum_{j=1}^{3} U_{i,j} + U_4 + U_5 + U_s - \mathbf{f}^T \mathbf{p} \tag{7}$$

The potential energy U depends on $\mathbf{q}_a$, $\mathbf{q}_d$, $\mathbf{p}$ and $\mathbf{f}$. It should be noted that coordinates $\mathbf{q}_a$, $\mathbf{q}_d$ and $\mathbf{p}$ depend on another due to the geometric constraints expressed through relations $\boldsymbol{\phi}(\mathbf{q}_a, \mathbf{q}_d, \mathbf{p}) = \mathbf{0}$ that must be verified for any configuration of the robot.

For our robot, there exists four geometric constraints grouped in $\boldsymbol{\phi} = \begin{bmatrix}\phi_{11} & \phi_{12} & \phi_{21} & \phi_{22}\end{bmatrix}^T$ $(i = 1, 2)$:

$$\begin{aligned}
\phi_{i1} = 0 &= \overrightarrow{OO_{i1}} \cdot \mathbf{x}_0 + \ell_{i1} \cos(q_{i1}) + \ell_{i2} \cos(q_{i1} + q_{i2}) \\
&\quad + \ell_{i3} \cos(q_{i1} + q_{i2} + q_{i3}) - x \\
\phi_{i2} = 0 &= \overrightarrow{OO_{i1}} \cdot \mathbf{z}_0 + \ell_{i1} \sin(q_{i1}) + \ell_{i2} \sin(q_{i1} + q_{i2}) \\
&\quad + \ell_{i3} \sin(q_{i1} + q_{i2} + q_{i3}) - z
\end{aligned} \tag{8}$$

Identifying stable solutions to DGSP A solution to the DGSP is found when the potential energy U is at a local minimum while the four geometric constraints (8) are verified. This can be formulated as the following constrained optimization problem:

$$\mathbf{q}_t = \arg\min U(\mathbf{q}_a, \mathbf{q}_d, \mathbf{p}, \mathbf{f}) \text{ subject to } \boldsymbol{\phi}(\mathbf{q}_a, \mathbf{q}_d, \mathbf{p}) = \mathbf{0} \tag{9}$$

where $\mathbf{q}_t$ was defined above as $\mathbf{q}_t = \begin{bmatrix}\mathbf{p}^T & \mathbf{q}_d^T\end{bmatrix}^T$. The force $\mathbf{f}$ and the coordinates $\mathbf{q}_a$ are considered fixed parameters.

This is a classical optimization problem which can be solved using the method of Lagrange multipliers. We therefore introduce the Lagrangian function $\mathscr{L} = U + \boldsymbol{\lambda}^T \boldsymbol{\phi}$, with $\boldsymbol{\lambda}$ the vector of Lagrange multipliers. The stationary points can then be found by solving the following equations with $\boldsymbol{\lambda}$ and $\mathbf{q}_t$ the unknowns:

$$\nabla_{\mathbf{q}_t} U(\mathbf{q}_a, \mathbf{q}_d, \mathbf{p}, \mathbf{f}) + \boldsymbol{\lambda}^T \nabla_{\mathbf{q}_t} \boldsymbol{\phi} = \mathbf{0}, \quad \boldsymbol{\phi}(\mathbf{q}_a, \mathbf{q}_d, \mathbf{p}) = \mathbf{0} \tag{10}$$

where $\nabla_{\mathbf{q}_t}$ designates the gradient with respect to the variables in $\mathbf{q}_t$.

However, at this stage, not all the obtained equilibrium configurations are stable. We therefore introduce the following second-order condition [21]:

$$\mathbf{H}^p = \mathbf{Z}^T \mathbf{H} \mathbf{Z} \succ 0 \tag{11}$$

in which:

- $\mathbf{H}$ is the Hessian of the Lagrangian obtained from the Hessian $\mathbf{H}^U_{\mathbf{q}_t}$ of the potential energy U with respect to the variable $\mathbf{q}_t$, and from the Hessians $\mathbf{H}^{\phi_k}_{\mathbf{q}_t}$ of the constraint ϕ_k with respect to the variables in $\mathbf{q}_t$, as follows:

$$\mathbf{H} = \mathbf{H}^U_{\mathbf{q}_t} + \sum_{k=1,4} \lambda_k \mathbf{H}^{\phi_k}_{\mathbf{q}_t} \tag{12}$$

- $\mathbf{Z}$ is the matrix which spans the null space of $\nabla_{\mathbf{q}_t} \boldsymbol{\phi}$, i.e.

$$\nabla_{\mathbf{q}_t} \boldsymbol{\phi}\ \mathbf{Z} = \mathbf{0} \tag{13}$$

Due to the complexity of the problem, an analytic solution could not be found. We therefore used a numerical approach to solve the DGSP.

Solver. In this section, we present the implementation of the optimization algorithm. The solver used is an interior point algorithm which takes advantage of the knowledge of the

analytic gradients and Hessian presented in the previous sections. Indeed, matrices $\nabla_{\mathbf{q}_t} U$, $\nabla_{\mathbf{q}_t} \boldsymbol{\phi}$, $\mathbf{H}^{U}_{\mathbf{q}_t}$ and $\mathbf{H}^{\phi_k}_{\mathbf{q}_t}$ were implemented analytically to help the solver to converge and to reduce the computation time. Their mathematical expressions are not given in this article. The initial point of the optimization ${\mathbf{q}_t^{(0)}}^T = \left[{\mathbf{p}^{(0)}}^T \ {\mathbf{q}_d{}^{(0)}}^T \right]^T$ is chosen randomly, with $\mathbf{p}^{(0)}$ chosen such that $x, z \in [-1,1]$ since this space includes all solutions satisfying the geometric constraints for the studied prototype (see section on workspace analysis), and with coordinates $\mathbf{q}_d{}^{(0)}$ chosen in the interval $[-\pi, \pi]$.

This optimization is carried out 100 times with a new choice of $\mathbf{q}_t^{(0)}$ at every iteration. We denote $\mathscr{S}(\mathbf{q}_a, \mathbf{f}) = \{\mathbf{q}_{t,m}\}_{m=1:n_s}$ the set of found solutions to the DGSP, with n_s the number of solutions.

Extending the solution set by continuity. The used optimization method is computationally costly and does not guarantee that all solutions will be found. In order to reduce the computation time, while increasing the probability to find all solutions, we use a method based on the prolongation by continuity of a solution. It was inspired from the method of continuation used in [22] to find the workspace boundaries of a planar tensegrity mechanism. Practically, if there exists a solution $\mathbf{q}_t^v \in \mathscr{S}(\mathbf{q}_a^v, \mathbf{f})$ in the vicinity of $\mathbf{q}_a$, that is not close to any of the found solutions $\mathbf{q}_t \in \mathscr{S}(\mathbf{q}_a, \mathbf{f})$, then this solution might be a missed solution. It is thus used as an initial point of a new optimization to help the algorithm converge to this neighbouring solution. A solution is considered close to another if $\max |\mathbf{q}_t^v - \mathbf{q}_t| < \varepsilon$, with ε a threshold.

3.2 Inverse Geometrico-Static Problem (IGSP)

The IGSP consists in finding all equilibrium and stable configurations $\mathbf{q}_{ad} = \left[\mathbf{q}_a^T \ \mathbf{q}_d^T\right]^T$ for a given position $\mathbf{p}$ of the end-effector and for a given external force $\mathbf{f}$ exerted on the end-effector. In this case, the equilibrium conditions can not be derived from the potential energy, since the compression of the preloaded bar is given by the position of the end-effector $\mathbf{p}$. We therefore study the equilibrium of forces at the end-effector. Our method is derived from one commonly used to compute the equilibrium configurations of a tensegrity mechanism, which consists in verifying the equilibrium of forces at each node [23].

Equilibrium conditions The total force at the level of the end-effector must be equal to zero ($\boldsymbol{\Sigma}_f = \mathbf{0}$) to guarantee the static equilibrium of the system. $\boldsymbol{\Sigma}_f$ is computed as follows (Fig. 3).

$$\boldsymbol{\Sigma}_f = \mathbf{f}_{13} + \mathbf{f}_{23} + \mathbf{f}_4 + \mathbf{f} \tag{14}$$

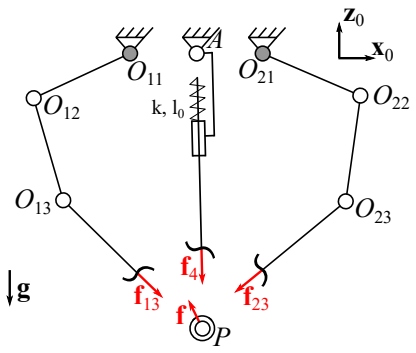

FIGURE 3: Balance of forces applied on the end-effector.

where:

- $\mathbf{f}_{i3}$ is the force exerted by the leg i on the end-effector;
- $\mathbf{f}_4$ is the force exerted by the preload bar on the end-effector;
- $\mathbf{f}$ is the force exerted by the environment on the end-effector.

The expressions of these forces are given in the following.

Forces of leg i. Assuming no external load is applied on the link ($i2$) or ($i3$) but gravity and joint forces, we apply the equilibrium of forces on each link of both passive legs. As a result, the force $\mathbf{f}_{i3}$ can be expressed as a function of $\theta_{i2} = q_{i1} + q_{i2}$ and $\theta_{i3} = q_{i1} + q_{i2} + q_{i3}$ under the following form:

$$\mathbf{f}_{i3}^T \, \mathbf{x}_0 = \frac{g(m_{i\alpha} - m_{i\beta})}{\tan(\theta_{i3}) - \tan(\theta_{i2})} \tag{15}$$

$$\mathbf{f}_{i3}^T \, \mathbf{z}_0 = \frac{g(m_{i\alpha}\tan(\theta_{i3}) - m_{i\beta}\tan(\theta_{i2}))}{\tan(\theta_{i3}) - \tan(\theta_{i2})} \tag{16}$$

with α_i and β_i, two masses defined as:

$$m_{i\alpha} = \left(\frac{\ell_{Si2}}{\ell_{i2}} m_{i2} + m_{i3} \right), \quad m_{i\beta} = m_{i3} \frac{\ell_{Si3}}{\ell_{i3}} \tag{17}$$

It should be noted that all components of the force $\mathbf{f}_{i3}$ become indeterminate when $\sin(q_{i3}) = 0$. In this case, the links $i2$ and $i3$ are aligned and the problem is ill-defined. This singularity should be analyzed in a further study.

Force of the preload system. Similarly, the force $\mathbf{f}_4$ applied by the preload system (Fig. 3) on the end-effector is:

$$\mathbf{f}_4^T \, \mathbf{x}_0 = -\left(k(\ell_0 - \rho_5) + \frac{\eta g}{\rho_5} \sin(q_4) \right) \cos(q_4) \tag{18}$$

$$\mathbf{f}_4^T \, \mathbf{z}_0 = -k(\ell_0 - \rho_5)\sin(q_4) + m_4 g + \frac{\eta g}{\rho_5} \cos(q_4)^2 \tag{19}$$

with:

$$\eta = \ell_{S4} m_4 + \ell_{S5} m_5 \tag{20}$$

Identifying stable configurations to IGSP Again, due to the complexity of the problem, we solve the IGSP through a numerical approach. The IGSP is formulated as an optimization problem, stated above:

$$\begin{aligned} \mathbf{q}_{ad} = \arg\min \Sigma_F(\mathbf{q}_a, \mathbf{q}_d, \mathbf{p}, \mathbf{f}) \text{ subject to } \boldsymbol{\phi}(\mathbf{q}_a, \mathbf{q}_d, \mathbf{p}) = \mathbf{0} \\ \text{and} \quad \boldsymbol{\Sigma}_F(\mathbf{q}_a, \mathbf{q}_d, \mathbf{p}, \mathbf{f}) = \mathbf{0} \end{aligned} \tag{21}$$

where $\mathbf{q}_{ad}$ was defined above as $\mathbf{q}_{ad} = \left[\mathbf{p}^T \ \mathbf{q}_d^T\right]^T$.

Similarly as what was done for the DGSP, the method used to solve this optimization problem is an interior point algorithm with analytic gradients and Hessian. The stability of the found equilibrium configuration is verified using the necessary condition: the projected Hessian given in Eq. (11) is positive definite.

In the next Section, the configurations reachable by prototype of R-Min robot are analyzed.

4 WORKSPACE COMPUTATION

In this section, we present the results obtained numerically to the direct (DGSP) and inverse (IGSP) problems. These methods are applied to the R-Min prototype [17] presented in Fig. 4. The associated link lengths, masses and centers of masses positions are given in Table 1.

4.1 Analysis of solutions to DGSP

In this section, we analyze the solutions found to the DGSP. In order to reduce the computation time, the analysis is conducted on a restricted joint space $\mathscr{Q}_a = \{\mathbf{q}_a | -\frac{\pi}{3} < q_{11} < \frac{2\pi}{3}, -\frac{\pi}{3} < \pi - q_{21} < \frac{2\pi}{3}, \pi - q_{21} < q_{11}\}$. The previous inequalities permit to reduce the studied joint space considering mechanical stops on both actuators and the symmetry of the robot. This restricted joint space $\mathscr{Q}_a$ is sampled with a resolution of $\pi/200$.

The number of solutions found to the DGSP for $\mathbf{q}_a \in \mathscr{Q}_a$, when no force is applied on the end-effector (i.e. $\mathbf{f} = \mathbf{0}$), is presented in Fig. 5.

This figure shows that the number of stable configurations for a given value of $\mathbf{q}_a$ varies from 0 (the robot assembly is not possible) to 4. In Figure 6, the robot is represented in four different configurations, each corresponding to a solution of the DGSP obtained for a particular value of $\mathbf{q}_a = \mathbf{q}_a^A = \left[4.574, 4.312\right]^T$, shown on Fig. 5. The first configuration Fig. 6(a) corresponds to a configuration desirable for manipulating a payload in a collaborative mode. The preload bar pushes the effector downwards, so that the passive arms are almost completely extended. Indeed, they are slightly folded due to gravity effects. The second configuration Fig. 6(b) could be interpreted as similar as the second assembly mode of the classical five-bar robot. In this case, the force exerted by the preload bar is directed upwards. The third equilibrium configuration is presented on Fig. 6(c). In this case, the right arm is folded over itself and the left arm is completely extended. A symmetric configuration, is presented on Fig. 6(d). Two other solutions of the DGSP are represented on Fig. 7 for another value $\mathbf{q}_a = \mathbf{q}_a^B = \left[5.202, 4.943\right]^T$. These solutions are

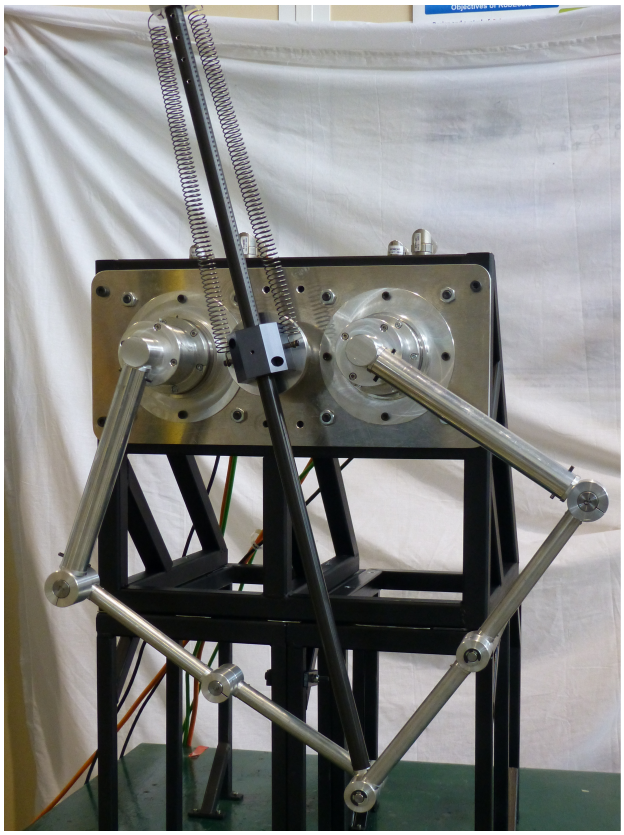

FIGURE 4: R-Min prototype

TABLE 1: Dimensions and mass properties of the prototype links

Link	Length	Mass	COM
$(i;j)$	ℓ_{ij} (m)	m_{ij} (kg)	ℓ_{Sij} (m)
(1&2;1)	0.28	1.29	0.0768
(1&2;2)	0.2	0.24	0.012
(1&2;3)	0.202	0.19	0.01
(-;4)	0.82	0.42	-0.31
(-;5)	-	0.81	0

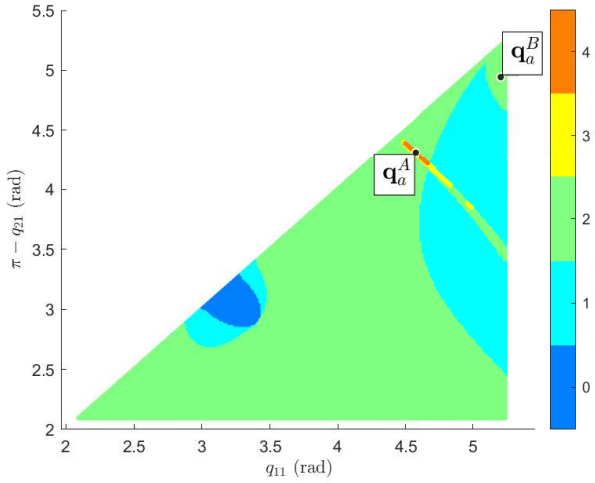

FIGURE 5: Number of solutions to the DGSP in the joint space in case no force is applied on the end-effector.

further analyzed in the next section.

Classification of solutions to DSGP Based on an exhaustive analysis of the set $\mathscr{S}_t$ of all solutions to the DGSP, we identified five different subsets of solution $\mathscr{S}_1$ to $\mathscr{S}_5$ in the joint space:

$$\begin{aligned}
\mathscr{S}_1 &= \mathscr{S}_t \cap C_1 \cap \bar{C}_3 \cap \bar{C}_4 \\
\mathscr{S}_2 &= \mathscr{S}_t \cap C_2 \cap C_3 \\
\mathscr{S}_3 &= \mathscr{S}_t \cap \bar{C}_2 \\
\mathscr{S}_4 &= \mathscr{S}_t \cap \bar{C}_1 \\
\mathscr{S}_5 &= \mathscr{S}_t \cap C_1 \cap \bar{C}_3 \cap C_4
\end{aligned} \tag{22}$$

in which the sub-spaces C_1 to C_4 are defined by using the following set of inequalities:

$$\begin{aligned}
C_1 &= \left\{ \mathbf{q}_t \in \mathbb{R}^6 \,\middle|\, -\frac{\pi}{2} < q_{13} < \frac{\pi}{2} \right\} \\
C_2 &= \left\{ \mathbf{q}_t \in \mathbb{R}^6 \,\middle|\, -\frac{\pi}{2} < q_{23} < \frac{\pi}{2} \right\} \\
C_3 &= \left\{ \mathbf{q}_t \in \mathbb{R}^6 \,\middle|\, -\pi < q_4 - \frac{q_{11}+q_{21}}{2} < 0 \right\} \\
C_4 &= \left\{ \mathbf{q}_t \in \mathbb{R}^6 \,|\, 0 < q_{23} < \pi \quad \textit{and} \quad -\pi < q_{21} < 0 \right\}
\end{aligned} \tag{23}$$

A projection of these subsets of solutions in the joint space (resp. Cartesian space) is presented in Fig. 8 (resp. Fig. 9) and detailed below:

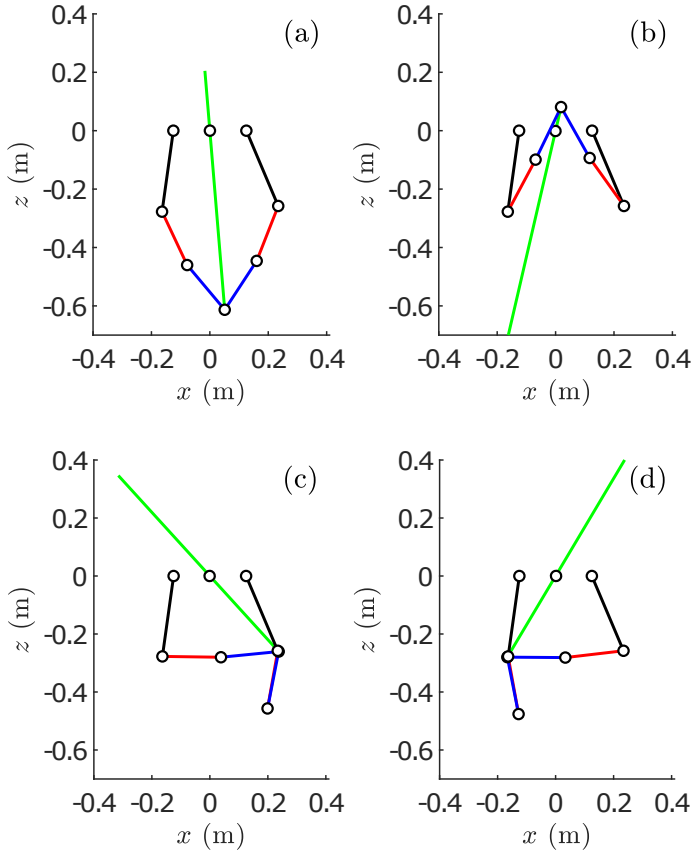

FIGURE 6: Representation of the four different configurations of the robot corresponding to the four solutions to the DGSP with $\mathbf{q}_a^A = [4.574, 4.312]^T$ and $\mathbf{f} = \mathbf{0}$.

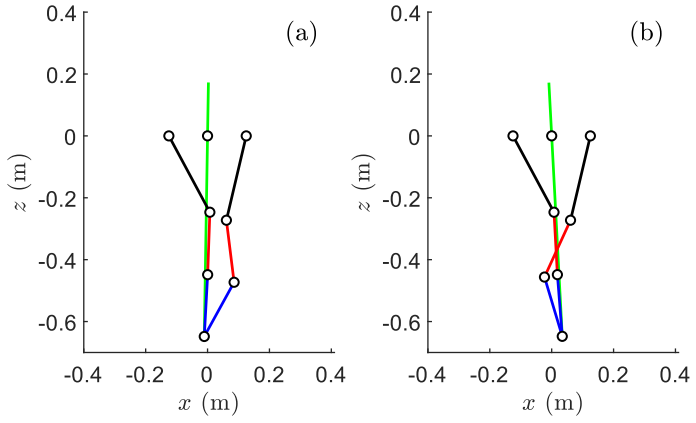

FIGURE 7: Representation of the two different configurations of the robot corresponding to the two solutions to the DGSP with $\mathbf{q}_a^B = [5.205, 4.943]^T$ and $\mathbf{f} = \mathbf{0}$.

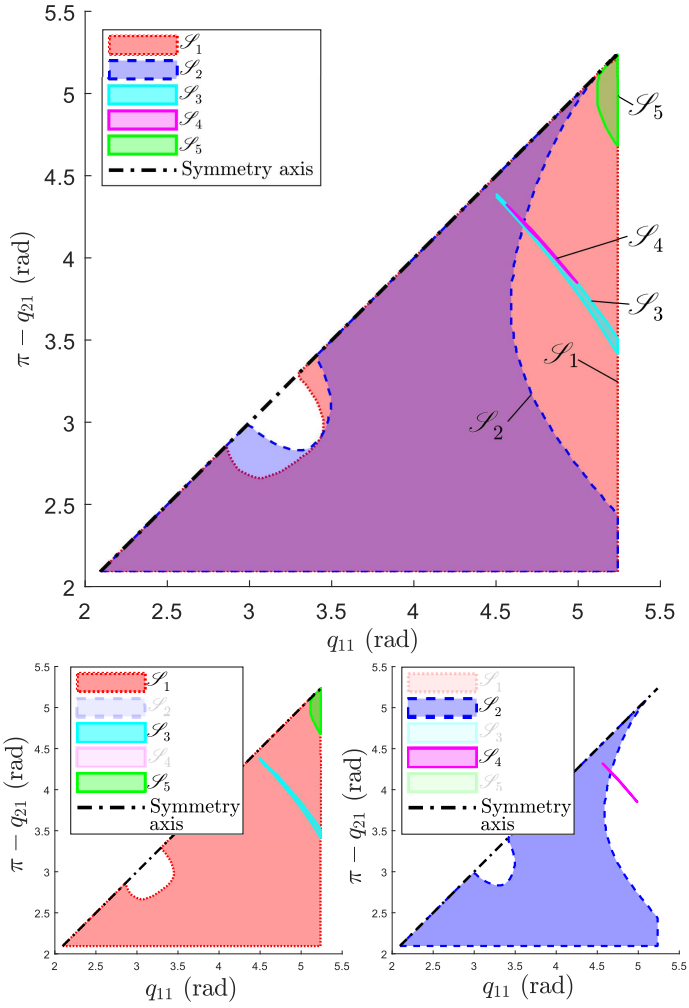

FIGURE 8: Contour of the subsets of DGSP solutions projected in the joint space.

- $\mathscr{S}_1$ corresponds to the configuration desired for collaborative manipulation of the robot as illustrated in Fig. 6.(a) or Fig. 7.(a), since both distal arms are extended and can thus fold in case of a collision with a human. Furthermore, it permits to obtain the largest workspace (see Fig. 9).
- $\mathscr{S}_2$ corresponds to the second assembly mode as illustrated in Fig. 6(b), the force exerted by the spring is here opposed to the gravity.
- $\mathscr{S}_3$ (resp. $\mathscr{S}_4$) corresponds to a configuration of the robot where the right arm (resp. the left arm) is completely folded like shown on Fig. 6(c) (resp. on Fig. 6(d)).
- $\mathscr{S}_5$ corresponds to a configuration where the angle q_{23} is negative (Fig. 7(b)).

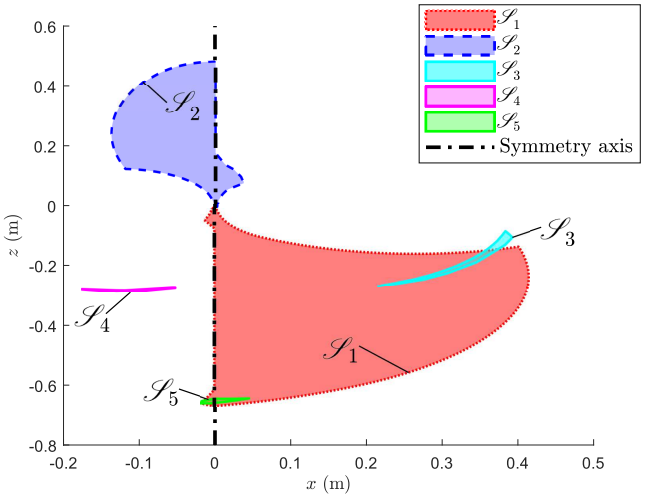

FIGURE 9: Contour of the subsets of DGSP solutions projected in the Cartesian space.

4.2 Analysis of solutions to IGSP

In this section, we analyze the solutions found to the IGSP for $\mathbf{f} = \mathbf{0}$ N. The search space is limited to $\mathscr{Q}_p = \{\mathbf{p} \,|0 < x < 0.6\,,\, -0.7 < z < 0\}$ ($x \geq 0$ since we consider the symmetry of the robot). The number of solutions to the IGSP for any $\mathbf{p} \in \mathscr{Q}_p$ is shown in Fig. 10.

In the same manner as the one for the study of the subsets of solutions to the DGSP, we identified subsets of solutions to the IGSP. We kept only one subset $\mathscr{T}$ that provides a configuration of the robot where both distal arms are extended and the preload bar lies between both distal arms, see Fig. 6(a). This subset $\mathscr{T}$ is defined with the following equation:

$$\mathscr{T} = \mathscr{T}_t \cap D_1 \cap D_2 \cap D_3 \cap D_4 \cap D_5 \tag{24}$$

with $\mathscr{T}_t$, the set of all solutions to the IGSP for $\mathbf{p} \in \mathscr{Q}_p$ and D_1 to D_5, a set of sub-spaces defined as:

$$\begin{aligned}
D_1 &= \left\{ \mathbf{q}_{ad} \in \mathbb{R}^6 \,\middle|\, -\frac{\pi}{2} < q_{13} < \frac{\pi}{2} \right\} \\
D_2 &= \left\{ \mathbf{q}_{ad} \in \mathbb{R}^6 \,\middle|\, -\pi < q_4 - \frac{q_{11}+q_{21}}{2} < 0 \right\} \\
D_3 &= \left\{ \mathbf{q}_{ad} \in \mathbb{R}^6 \,|0 < q_{12}+q_{13} < \pi \quad \right\} \\
D_4 &= \left\{ \mathbf{q}_{ad} \in \mathbb{R}^6 \,|-\pi < q_{22} < 0 \quad \right\} \\
D_5 &= \left\{ \mathbf{q}_{ad} \in \mathbb{R}^6 \,|q_a \in \mathscr{Q}_a \right\}
\end{aligned} \tag{25}$$

This type of configuration is desirable for multiple reasons:

- both distal arms can fold in case of a collision with a human,

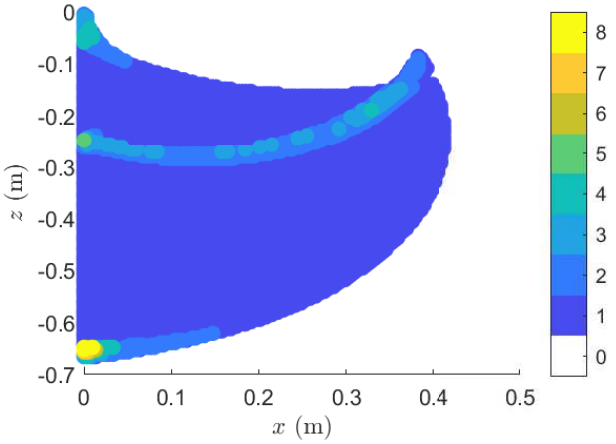

FIGURE 10: Number of IGSP solutions for a given position of the Cartesian space, in case no force is applied on the end-effector.

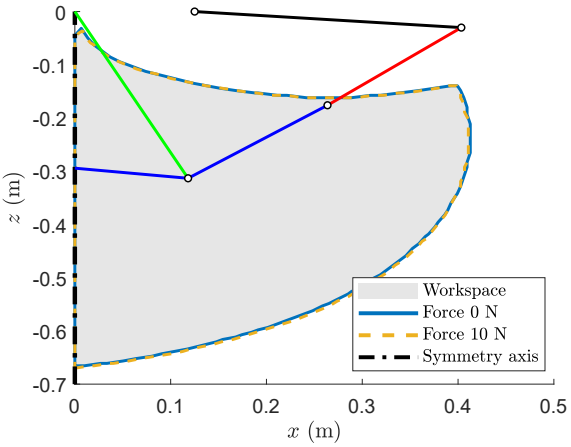

FIGURE 11: Contour of the Cartesian workspace corresponding to the projection of a single subset of solutions to the IGSP. The workspace is plotted for two cases, when no force is applied on the end-effector and when a force of 10N is applied downwards.

- the preload bar does not present any risk of injury since it lies between both distal arms and thus can not enter in contact with anybody,
- it offers the largest projection in the cartesian space,
- the weight of the payload has no (or little) effect on the position of the end-effector.

The obtained workspace is represented on Fig. 11. It corresponds to the projection of the selected subset $\mathscr{T}$ of solutions to the IGSP in the Cartesian space. This workspace has been analyzed for forces $\mathbf{f}$ directed downwards, and equal to 0, 2, 4, 6, 8, 10 N. It can be seen, that the boundaries of the workspace are not much affected when the payload varies from 0 to 10 N, making this robot well-adapted to manipulation tasks. Analyses of the workspace for higher payloads or forces directed in other directions are left as future works.

5 CONCLUSIONS

In this paper, we introduced the geometrico-static analysis of an intrinsically safe parallel manipulator for fast pick-and-place operations, called R-Min. R-Min has been designed so that the risk of injury during a collision with a human operator is reduced, while maintaining high speed and acceleration capacities. The proposed architecture is based on an underactuated parallel kinematic chain constrained by a mechanical preload system mounted between the base and the end-effector. The robot is thus able to passively self-reconfigure during a collision.

Because the robot is underactuated, its equilibrium configurations do not only rely on the geometric constraints but also on gravitational effects, external forces and stiffness of the preload bar. A geometrico-static model of the robot was thus introduced in order to solve the direct and inverse problems. In both cases, 2^{nd} order conditions were used to check the stability of the obtained equilibrium solutions. Due to the complexity of expressions, solutions to both problems were obtained using a numerical approach. The number of solutions to the direct problem, when no force is exerted on the end-effector, was shown to vary from 0 to 4. We then introduced multiple sets of inequalities to classify these solutions into independent subsets of continuous solutions. In the same manner, the number of solutions to the inverse problem was shown to vary from 0 to 8. We identified the solution that is desirable for the robot to operate in a safe manipulation mode. This solution provides a configuration where both distal arms are extended, they can thus fold in case of a collision with a human. Furthermore, the projection of this subset of solutions in the Cartesian space offers a large workspace which is not much affected when the payload varies from 0 to 10 N. Future works will include experiments on the designed prototype, singularity analysis and optimal design based on safety criteria.

ACKNOWLEDGMENT

We would like to thank Ghislain Jeanneau for the help in finding an elegant way to program the prolongation by continuity. This work was supported by ENS Rennes.

REFERENCES

[1] Haddadin, S., De Luca, A., and Albu-Schäffer, A., 2017. "Robot collisions: A survey on detection, isolation, and

identification". *IEEE Transactions on Robotics,* ***33***(6), pp. 1292–1312.

[2] ISO/TS15066 : Robots and robotic devices – Collaborative robots.

[3] Meguenani, A., Padois, V., Da Silva, J., Hoarau, A., and Bidaud, P., 2016. "Energy based control for safe human-robot physical interaction". In International Symposium on Experimental Robotics, Springer, pp. 809–818.

[4] Hirzinger, G., Sporer, N., Albu-Schaffer, A., Hahnle, M., Krenn, R., Pascucci, A., and Schedl, M., 2002. "DLR's torque-controlled light weight robot iii-are we reaching the technological limits now?". In Proceedings 2002 IEEE International Conference on Robotics and Automation (Cat. No. 02CH37292), Vol. 2, IEEE, pp. 1710–1716.

[5] Kim, Y. J., 2017. "Anthropomorphic low-inertia high-stiffness manipulator for high-speed safe interaction". *IEEE Transactions on Robotics,* ***33***(6), pp. 1358–1374.

[6] Pratt, G. A., and Williamson, M. M., 1995. "Series elastic actuators". In Proceedings 1995 IEEE/RSJ International Conference on Intelligent Robots and Systems. Human Robot Interaction and Cooperative Robots, Vol. 1, IEEE, pp. 399–406.

[7] Bicchi, A., and Tonietti, G., 2004. "Fast and" soft-arm" tactics [robot arm design]". *IEEE Robotics & Automation Magazine,* ***11***(2), pp. 22–33.

[8] Yoon, S.-S., Kang, S., Yun, S.-k., Kim, S.-J., Kim, Y.-H., and Kim, M., 2005. "Safe arm design with MR-based passive compliant joints and visco—elastic covering for service robot applications". *Journal of mechanical science and technology,* ***19***(10), pp. 1835–1845.

[9] Eiberger, O., Haddadin, S., Weis, M., Albu-Schäffer, A., and Hirzinger, G., 2010. "On joint design with intrinsic variable compliance: Derivation of the DLR QA-joint". In 2010 IEEE International Conference on Robotics and Automation, IEEE, pp. 1687–1694.

[10] Wolf, S., Eiberger, O., and Hirzinger, G., 2011. "The DLR FSJ: Energy based design of a variable stiffness joint". In 2011 IEEE International Conference on Robotics and Automation, IEEE, pp. 5082–5089.

[11] Park, J.-J., Kim, B.-S., Song, J.-B., and Kim, H.-S., 2008. "Safe link mechanism based on nonlinear stiffness for collision safety". *Mechanism and Machine Theory,* ***43***(10), pp. 1332–1348.

[12] Lauzier, N., and Gosselin, C., 2012. "Performance indices for collaborative serial robots with optimally adjusted series clutch actuators". *Journal of Mechanisms and Robotics,* ***4***(2), p. 021002.

[13] López-Martínez, J., Blanco-Claraco, J. L., García-Vallejo, D., and Giménez-Fernández, A., 2015. "Design and analysis of a flexible linkage for robot safe operation in collaborative scenarios". *Mechanism and Machine Theory,* ***92***, pp. 1–16.

[14] Seriani, S., Gallina, P., Scalera, L., and Lughi, V., 2018. "Development of n-dof preloaded structures for impact mitigation in cobots". *Journal of Mechanisms and Robotics,* ***10***(5), p. 051009.

[15] Lauzier, N., and Gosselin, C., 2010. "3-dof cartesian force limiting device based on the delta architecture for safe physical human-robot interaction". In 2010 IEEE International Conference on Robotics and Automation, IEEE, pp. 3420–3425.

[16] Campa, F., Diez, M., Diaz-Caneja, D., and Altuzarra, O., 2019. "A 2 dof continuum parallel robot for pick & place collaborative tasks". In IFToMM World Congress on Mechanism and Machine Science, Springer, pp. 1979–1988.

[17] Jeanneau, G., Bégoc, V., Briot, S., and Goldsztejn, A., 2020. "R-Min: a fast collaborative underactuated parallel robot for pick-and-place operations". In 2020 IEEE International Conference on Robotics and Automation, IEEE.

[18] Gao, D., and Wampler, C. W., 2009. "Head injury criterion". *IEEE robotics & automation magazine,* ***16***(4), pp. 71–74.

[19] Campos, L., Bourbonnais, F., Bonev, I. A., and Bigras, P., 2011. "Development of a five-bar parallel robot with large workspace". In ASME 2010 International Design Engineering Technical Conferences and Computers and Information in Engineering Conference, American Society of Mechanical Engineers Digital Collection, pp. 917–922.

[20] Birglen, L., Laliberté, T., and Gosselin, C. M., 2007. *Underactuated robotic hands*, Vol. 40. Springer.

[21] Nocedal, J., and Wright, S. J., 2006. "Theory of constrained optimization". *Numerical optimization*, pp. 304–354.

[22] Boehler, Q., Charpentier, I., Vedrines, M. S., and Renaud, P., 2015. "Definition and computation of tensegrity mechanism workspace". *Journal of Mechanisms and Robotics,* ***7***(4).

[23] Skelton, R. E., and de Oliveira, M. C., 2009. *Tensegrity systems*, Vol. 1. Springer.